Petroleum Science 20 (2023) 2545–2553

Contents lists available at ScienceDirect

Petroleum Science

journal homepage: www.keaipublishing.com/en/journals/petroleum-science

Original Paper

A novel synthesis of highly active and highly stable non-noble-nickel-modified persulfated Al_2O_3@ZrO_2 core-shell catalysts for *n*-pentane isomerization

Tian-Han Zhu [a, b], Mei Zhang [a, **], Sheng-Nan Li [a], Feng Li [a], Hua Song [a, *]

[a] Provincial Key Laboratory of Oil & Gas Chemical Technology, College of Chemistry & Chemical Engineering, Northeast Petroleum University, Daqing, Heilongjiang, 163318, China
[b] Guangzhou Institute of Energy Conversion, Chinese Academy of Sciences, Guangzhou, Guangdong, 510640, China

ARTICLE INFO

Article history:
Received 13 June 2022
Received in revised form
11 October 2022
Accepted 22 February 2023
Available online 4 March 2023

Edited by Jia-Jia Fei

Keywords:
Core-shell
Large pore size
Solid superacid
Non-noble metal Ni
Isomerization

ABSTRACT

The non-noble metal modified sulfated zirconia was found easy to deactivate. Herein, highly active and highly stable non-noble core-shell Ni-$S_2O_8^{2-}$/Al_2O_3@ZrO_2 catalysts (Ni-SA@Z-*x*, *x* = Al content in wt%) have been successfully prepared and investigated for *n*-pentane isomerization. The results showed that the core-shell Ni-SA@Z-30 provided a sustained high isopentane yield (63.1%) with little or no deactivation within 5000 min at a mild reaction pressure of 2.0 MPa, which can be attributed to the following factors: (i) carbon deposition was greatly suppressed by the large pore size and huge pore volume; (ii) the loss of sulfur entities was suppressed because the small and highly dispersed tetragonal ZrO_2 particles can bond with the S species strongly; (iii) strong Brønsted acidity can be maintained well after the isomerization. The pore structures and acid nature of the core-shell Ni-SA@Z-*x* are entirely different from those of the normal structure Ni-$S_2O_8^{2-}$/ZrO_2-Al_2O_3, even though the Al content and the compositions of the individual components are the same. The Al_2O_3 cores endow the catalysts with high internal surface area and high mechanical strength. Meanwhile, the ZrO_2 shell, which consists of more and smaller tetragonal ZrO_2 particles because of the large surface area of the Al_2O_3 core, promotes the formation of more stable sulfur species and stronger binding sites.

1. Introduction

The catalytic hydroconversion of *n*-paraffins is an important reaction to improve the quality of diesel and gasoline in the oil-refining industry (Zhou et al., 2022). Hydroisomerization of light alkane can produce high-octane fractions for gasoline blending with non-aromatic hydrocarbons to meet increasingly stringent environmental protection regulations (Zhan et al., 2022). Environmentally friendly solid superacid catalysts, especially for sulfated zirconia (SZ)-based samples, have been regarded as the most promising candidates for preparation of isomerization catalysts with high catalytic activity at low reaction temperature (Wang et al., 2020). However, the catalytic performance of pristine SZ is known to be unacceptable caused by the rapid deactivation in practical application. Therefore, the dopants of noble metals (Pt, Pd) and/or various transition metals (Fe, Ni, Mn, and Cu) have been adopted to modify the catalyst and results in much higher activity than that of raw SZ (Lyu et al., 2021; Song et al., 2015). Typically, the Ni belongs to the same family of Pd and Pt, more and more attentions have been paid to design low-cost Ni-modified SZ catalyst for replacement of noble metal. Though, the Ni-SZ catalyst exhibits acceptable isomerization activity at low temperature, the deactivation is also needed to be taken into consideration (Song et al., 2016a). Reasons for deactivation of SZ-based catalysts have been reported to be complex (Liu et al., 2020; Wang et al., 2016; Kim et al., 2000; Li and Stair, 1996), such as coke deposition (Li et al., 2006), leach of sulfate species (Ng and Horvát, 1995), change in surface acidity (González et al., 1997) and phase transition from tetragonal to monoclinic zirconia (Li and Stair, 1996). Therefore, it is of great of interest to design non-noble metal modified SZ catalysts with high catalytic activity and stability.

* Corresponding author.
** Corresponding author.
E-mail addresses: zhangmei8132@126.com (M. Zhang), songhua2004@sina.com (H. Song).

https://doi.org/10.1016/j.petsci.2023.02.027

Recently, many efforts have been made to alleviate the deactivation and the introduction of alumina into SZ are found to improve the catalytic activity and stability for isomerization performance (Hua et al., 2000; Gao et al., 1998). The modification of alumina contributed to the enhanced concentration of active sites and acid sites. Furthermore, the addition of alumina can retard the crystal phase transformation of ZrO_2 from tetragonal to monoclinic phase (Zhou et al., 2021; Wang et al., 2022). As compared to intrinsic Pt-SO_4/ZrO_2 catalyst, the alumina-modified sample exhibited higher pore volume and specific surface area, more importantly, the alumina resulted in enhanced stability of tetragonal zirconia, which contributed to an excellent stability and activity for light naphtha isomerization (Zhou et al., 2022). Our previous research (Song et al., 2014) also found that the addition of an appropriate amount of Al (2.5 wt% of Al) can increase the amount of acid sites and the surface area, suppressing the phase transformation of tetragonal ZrO_2 to monoclinic ZrO_2. But an excessive amount of Al would decrease the number of surface tetragonal ZrO_2 particles and led to a decrease in the formation of acid sites, which was generated by sulfate species adsorbed on the stepped edges of tetragonal ZrO_2, and thus resulted in a significant decrease in activity. Therefore, the complete utilization of the skeleton structure and acid nature of γ-Al_2O_3 support is limited due to the low Al content of < 5 wt%. Considering the disadvantages, the as-prepared catalyst often exhibited poor stability caused by the deactivation of SZ (Song et al., 2016b).

Generally, the pore structure and acidity of the support played a vital role on the coke deposition during *n*-alkane isomerization. For example, the pore with large size can facilitate the mass transfer, which reduces the residence time of hydrocarbon compounds on the catalyst surface and suppresses the deposition of carbon. Recently, core-shell structure materials have attracted worldwide attention due to their unique physical and chemical properties (Das et al., 2021). The core-shell nanoparticles exhibit many advantages, such as tunable surface modification, improved functionality, enhanced stability by protecting the active phase from contact with poisoning substances, lower consumption of precious materials, and so on (Gao et al., 2021). However, to the best of our knowledge, few studies have been reported concerning the use of γ-Al_2O_3 as a core support material for preparation of superacid SZ catalysts.

Herein, a method for preparing highly active and highly stable non-noble-nickel-modified persulfated Al_2O_3@ZrO_2 core-shell catalyst (Ni-$S_2O_8^{2-}$/Al_2O_3@ZrO_2) was proposed to make full use of the respective advantages of Al_2O_3 and ZrO_2. The Al_2O_3 core can impart the core-shell structure materials with high internal surface area and high mechanical strength for the support, which contributes to the formation of external shell with more and smaller tetragonal ZrO_2 particles. As a result, the formation of superacid sites is accelerated due to the intimate contact between Zr and S species. Besides, the Al_2O_3 endows additional acid sites for the core-shell support and stabilizes the active tetragonal phase of ZrO_2, which is also responsible for the improved catalytic performance. In the case of *n*-pentane isomerization, the core-shell Ni-$S_2O_8^{2-}$/Al_2O_3@ZrO_2 catalyst showed a high isopentane yield (63%) with little or no deactivation within 5000 min. To the best of our knowledge, such a non-noble superacid catalyst with high isopentane yield and excellent stability at a low pressure (2.0 MPa) is extremely unusual.

2. Experimental

2.1. Synthesis methods

The Al_2O_3@ZrO_2 (core@shell, A@Z) supports were synthesized by deposition of zirconia on the γ-Al_2O_3. In a typical procedure, a certain amount of γ-Al_2O_3 and butanol were mixed at room temperature, and deionized water was added dropwise to the suspension under vigorous stirring for further dispersion. Then, the calculated amount of zirconium (IV) butoxide was dissolved into the resulting suspension with different Zr/Al mass ratio, and stirred for another 30 min. Subsequently, the suspension was transferred into autoclaves for hydrothermal reaction at 443 K for 24 h. After cooling down to room temperature, the obtained products were separated by centrifugation, and then dried at 353 K for 24 h to obtain the A@Z-*x* samples, where *x* represented the percentage of Al content. Then the product was re-dispersed into a 0.75 M $(NH_4)_2S_2O_8$ solution and stirred for 15 min. After aging for 6 h, the samples were separated by centrifugation and dried at 353 K for 24 h to obtain the SA@Z-*x* samples.

The supported core@shell nickel catalysts (Ni-SA@Z-*x*) were prepared by the incipient wetness impregnation method (Song et al., 2015). Typically, calculated amount of the SA@Z-*x* material and $Ni(NO_3)_2 \cdot 6H_2O$ were added into 10 mL deionized water. Then the obtained samples were dried at 373 K for 12 h and calcined at 923 K for 3 h to obtain the Ni-SA@Z-*x* with Ni loading of 1.0 wt%.

According to our previous study (Song et al., 2014), Pd-SZA catalyst made from Al content of 2.5 wt% exhibited the best performance. Therefore, for comparison the common SZA with Al_2O_3 content of 2.5 wt% was chosen to synthesize the supported Ni catalyst with Ni loading of 1.0 wt%. And the obtained catalyst was designed as Ni-SZA-2.5.

2.2. Characterization methods

X-ray powder diffraction (XRD) patterns were recorded on a D/max-2200PC X-ray diffractometer (40 kV, 40 mA) fitted with Cu Kα radiation (0.15404 nm). N_2-adsorption was measured at 77 K using Micromeritics ASAP 2460 analyzer to obtain the microporous and mesoporous porosities, respectively. Transmission electron microscope (TEM) examinations were performed using the JEM-2010 instrument supplied by JEOL. Scanning electron microscope (SEM) with an acceleration voltage of 10 kV was conducted using Zeiss SIGMA equipment. Thermogravimetric analysis (TG) was performed on the samples (10 mg) after reaction using a PerkinElmer Diamond instrument under air with a flow rate of 100 mL min^{-1}, from room temperature to 1123 K, and with a heating rate of 10 K min^{-1}. Fourier transform infrared spectroscopy (FT-IR) measurements were carried out with a Bruker Tensor 27 FT-IR spectrometer. Fourier transform infrared spectroscopy of pyridine adsorption (Py-IR) was recorded on a Spectrum GX Fourier by adding 64 scans for the sample at a resolution of 4 cm^{-1}. The metal loadings of the samples were determined by X-ray fluorescence (XRF) with a spectrometer XRF-1800. XPS were acquired with a PHI-1600 spectrometer equipped with a hemispherical electron analyzer and a Mg Kα (1253.6 eV) X-ray source.

2.3. Catalytic performance

The isomerization reaction of *n*-pentane was chosen to evaluate the catalytic activity of the prepared catalysts. The reactions were performed in a fixed-bed flow reactor. Prior to reaction, 2 g of the catalyst was activated with flowing H_2 stream (20 mL min^{-1}) at 573 K for 3 h, and then cooled to the reaction temperature. The reaction conditions were set to a weight hourly space velocity (WHSV) of 1 h^{-1}, an H_2/*n*-pentane mole ratio of 4.0, a total pressure of 2.0 MPa and a temperature ranging from 433 to 533 K. The reaction products were analyzed by an online FL9790 gas chromatograph equipped with a FID detector.

3. Results and discussion

3.1. XRD

The XRD patterns of fresh and spent samples were shown in Fig. 1. As depicted in Fig. 1(a), all samples showed the diffraction peaks at $2\theta = 30.3°$, 35.3°, 50.4° and 60.4°, which were related to the (101), (110), (112) and (211) planes of tetragonal ZrO_2, respectively (Reddy et al., 2018). The crystalline of tetragonal ZrO_2 was affected by the dopant of Al, the diffraction peak of tetragonal ZrO_2 was broadened with the increased Al content from 2.5 to 50 wt%, indicating the decreased crystalline size of zirconia particles with incremental Al content. The absence of Al_2O_3 peaks in Ni-SA@Z-*x* with the high Al content of 30–50 wt% proved that Al_2O_3 core was totally coated by ZrO_2 shell (Yang et al., 2013), suggesting the successful preparation of core-shell material. Besides, no crystalline phase of nickel oxide was detected due to the low content or high dispersion of nickel. Compared with the pattern of traditional Ni-SZA-2.5, the peak intensity of tetragonal ZrO_2 decreased remarkably for all Ni-SA@Z-*x* catalysts, indicating that the core-shell structure can effectively suppress the growth of crystalline zirconia particles and result in much smaller particles size of zirconia even at the same Al content of 2.5 wt%.

As shown in Fig. 1(b), the diffraction peaks of monoclinic ZrO_2 was detected for spent Ni-SZA-2.5 and Ni-SA@Z-2.5, which indicated the transformation of ZrO_2 from the metastable tetragonal to the monoclinic phase during the isomerization reaction. Generally, the binary ZrO_2/Al_2O_3 composite was often prepared by traditional sol-gel method and resulted in the uniform dispersion of Al and Zr species on the surface of binary nanocomposite, which led to the higher crystallizing temperature of tetragonal ZrO_2 caused by the addition of Al_2O_3 (Zhao et al., 2007; Liu et al., 2012). Alternatively, the core-shell structure SA@Z showed advantages than ZrO_2/Al_2O_3 composite, since the Al_2O_3 was totally covered by active tetragonal ZrO_2 phase. What's more, the tetragonal ZrO_2 phase has been reported to be necessary for isomerization performance (Liu et al., 2012). Besides, the monoclinic phase peaks of the spent Ni-SA@Z-*x* ($x = 30–50$) were very weak, suggesting the more stable tetragonal structure as compared to Ni-SA@Z-2.5 and higher catalytic stability in the case of *n*-pentane isomerization.

The crystal sizes of tetragonal zirconia for all samples were calculated by the Debye-Scherrer equation and listed in Table 1. Compared to traditional Ni-SZA-2.5 (9.7 nm), all Ni-SA@Z-*x* samples showed smaller crystallite size with increased Al addition. In detail, the tetragonal ZrO_2 crystallite size of Ni-SA@Z-*x* decreased from 8.2 to 4.9 nm (decreased by 40.2%) with the increased Al content from 2.5 to 50 wt%, indicating the positive effect of Al species on the formation of tetragonal ZrO_2 crystallite with smaller size. Similar result has been reported by Zarubica et al. (2021), an increase in Al content promoted the stabilization of smaller tetragonal ZrO_2 particles on the surface. As mentioned, the core-shell structure was beneficial to the formation of smaller tetragonal ZrO_2 particles, which also accelerated the contact between Zr and S species to form Zr–S bonds and deduced the formation of a superacid structure and dispersion of active sites and acid sites. This will be further discussed in Sections 3.5 and 3.6. Besides, the ZrO_2 crystallite size of Ni-SA@Z-*x* samples with 2.5~50 wt% Al content increased about 1.6–0.7 nm after reaction, which was still much lower than that of Ni-SZA-2.5. This further confirmed that the core-shell structure could restrain sintering of the tetragonal ZrO_2 phase and remain the integrity of its microscopic structure.

3.2. BET

The N_2 adsorption-desorption isotherms and pore size distributions of the catalysts were shown in Fig. S1. Accordingly, all the isotherms showed a type IV characteristic feature of isotherm, indicating the presence of some mesopores (Thommes et al., 2015). Ni-SZA-2.5 showed a narrow pore size distribution centered at around 3 nm. The Ni-SA@Z-2.5 showed a broader pore size distribution from 5 to 10 nm, and the main peak was close to that of γ-Al_2O_3. With increasing Al content, the pore size increased remarkably owing to the abundant Al provided more mesopores, and some of the micropores gradually merged into mesopores.

In comparison with Ni-SZA-2.5 (95.1 $m^2\ g^{-1}$), the Ni-SA@Z-2.5 showed a slightly higher specific surface area (S_{BET}) of 99.5 $m^2\ g^{-1}$ (Table 1). In addition, the pore size (D_p) increased remarkably from 3.7 to 5.6 nm, and the pore volume (V_{Total}) increased from 0.089 to 0.103 $cm^3\ g^{-1}$. This showed that the pore structures of these two catalysts were entirely different, even though the Al content and the compositions of the individual components are the same. The large D_p and V_{Total} of Ni-SA@Z-2.5 would enhance the diffusion rates of reactant and products. In particular, branched or large-sized products could pass through the pores more easily, suppressing carbon deposition on the surface of the catalyst. This would effectively arrest catalyst deactivation since carbon deposition is one of the main reasons for deactivation of catalysts of this kind (Song et al., 2016b). In addition, the large D_p and V_{Total} are also beneficial to the isomerization reaction. With increasing the Al content, the S_{BET}, V_{Total} and D_p of Ni-SA@Z-*x* increased remarkably. It is worth noting that the D_p and V_{Total} of Ni-SA@Z-50 were 2.1 and 4.2 times higher than those of Ni-SA@Z-2.5, respectively.

For Ni-SZA-2.5, S_{BET}, V_{Total} and D_p was dramatically decreased after reaction. The narrowed D_p indicated that carbon deposition

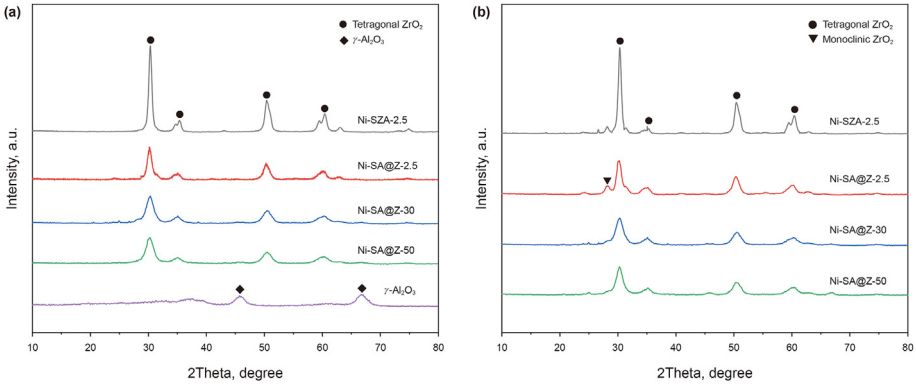

Fig. 1. XRD patterns of (**a**) fresh and (**b**) spent Ni-SZA-2.5 and Ni-SA@Z-*x* catalysts.

Table 1
Texture properties of fresh and spent catalysts.

Sample	S_{BET}, $m^2\ g^{-1}$			V_p, $cm^3\ g^{-1}$			D_p, nm	$D_{t\text{-}ZrO2}$, nm
	S_{BET}	S_{micro}	S_{meso}	V_{Total}	V_{micro}	V_{meso}		
Ni-SZA-2.5	95.1	41.9	53.2	0.089	0.067	0.022	3.7	9.7
Ni-SA@Z-2.5	99.5	40.1	59.4	0.103	0.012	0.091	5.6	8.2
Ni-SA@Z-30	122.1	36.6	85.5	0.214	0.009	0.205	6.9	5.4
Ni-SA@Z-50	135.1	33.6	101.5	0.429	0.007	0.422	12.0	4.9
Ni-SA@Z-70	155.5	30.0	125.5	0.478	0.007	0.471	8.6	6.1
Spent Ni-SZA-2.5	40.6	18.9	21.7	0.061	0.053	0.008	3.0	13.1
Spent Ni-SA@Z-2.5	70.5	28.4	42.1	0.102	0.016	0.086	5.5	9.8
Spent Ni-SA@Z-30	94.7	39.5	55.2	0.188	0.012	0.176	5.8	6.1
Spent Ni-SA@Z-50	100.4	37.2	63.2	0.350	0.010	0.340	10.1	5.6
Spent Ni-SA@Z-70	103.2	42.3	61.1	0.329	0.020	0.309	6.3	4.7

* Crystal sizes of tetragonal ZrO_2 calculated by the Debye-Scherrer equation.

mainly occurred inside the pores during the reaction. The deposited carbon would have coated the active metal sites and acid sites on the surface of the catalyst, leading to its deactivation. However, a slight decline in textural parameter of Ni-SA@Z-*x* catalysts was observed after reaction.

3.3. TEM

Fig. 2 exhibited the TEM images of Ni-SZA-2.5, Ni-SA@Z-2.5 and Ni-SA@Z-50 catalysts. Mokari et al. (2005) proposed that Zr particles may be easily identified by their dark contrast in TEM, as a result of the electron density contrast between Al and Zr. Moreover, because of low content and high dispersion, Ni particles could not be observed (Nichele et al., 2012). It can be seen from Fig. 2(a), (c) that the ZrO_2 particle size in the Ni-SZA-2.5 catalyst was approximately 8.4 nm with interplanar distances of 0.295 nm for ZrO_2 (101) plane (Bang et al., 2020). In Fig. 2(b), a light-color core surrounded by a dark shell can be clearly discerned. This indicated that a core-shell structure had been successfully synthesized. Besides, the core-shell structure of SA@Z-30 materials was also detected in SEM images (Fig. S2). The ZrO_2 particle size in the core-shell Ni-SA@Z-2.5 catalyst was about 6.7 nm (Fig. 2(d)), smaller than that of Ni-SZA-2.5, implying that the core-shell structure was beneficial to the formation of smaller tetragonal ZrO_2 particles. This observation was consistent with the XRD results (Table 1). For Ni-SA@Z-50, the Zr particle size decreased to about 3.9 nm with further increased Al content, indicating the positive effect of Al on dispersion of Zr species.

3.4. TG

The TG results of samples were shown in Fig. 3. All samples display weight loss in the range of room temperature to 938 K, which is attributed to desorption of physically and chemically adsorbed water molecules and the dihydroxylation process on the surface of ZrO_2 (Arkatova, 2010; Joo et al., 2013). Significant weight loss was clearly started at 938 K, which could be attributed to the decomposition of persulfate species with the evolution of sulfur dioxide, similar results have been reported elsewhere (Kim et al., 2006; Satam and Jayaram, 2008). Compared with Ni-SZA-2.5, the

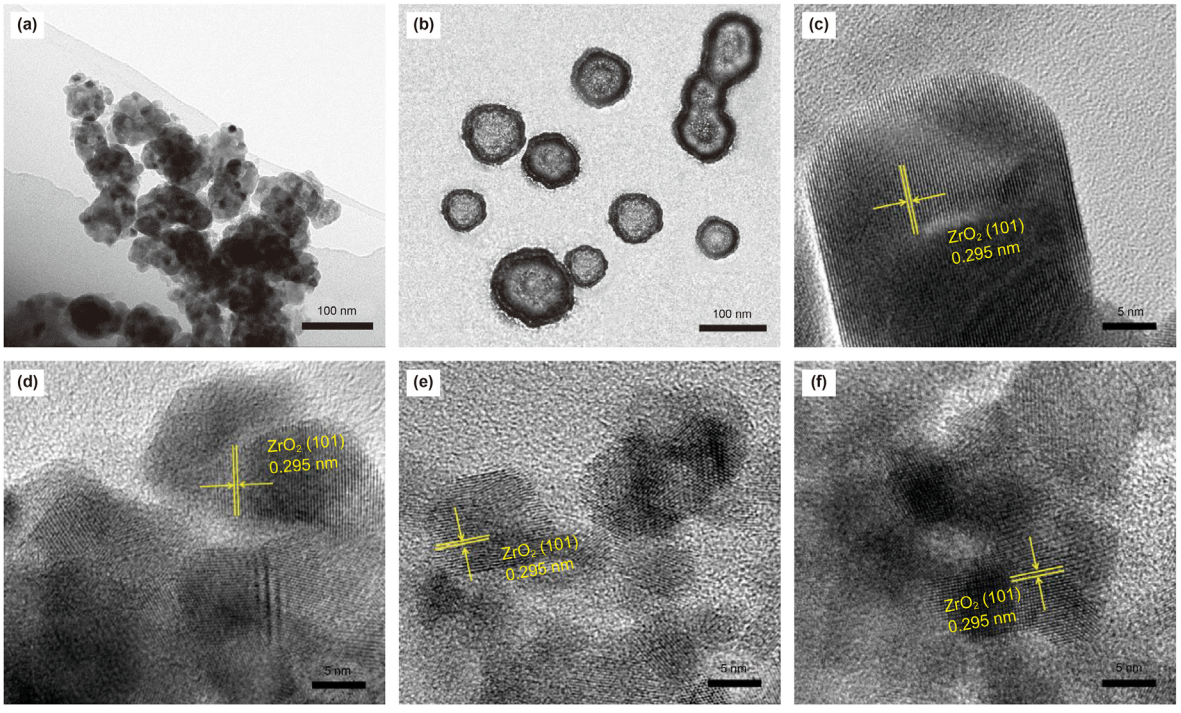

Fig. 2. TEM of (**a**, **c**) Ni-SZA-2.5, (**b**, **e**) Ni-SA@Z-30, (**d**) Ni-SA@Z-2.5 and (**f**) Ni-SA@Z-50.

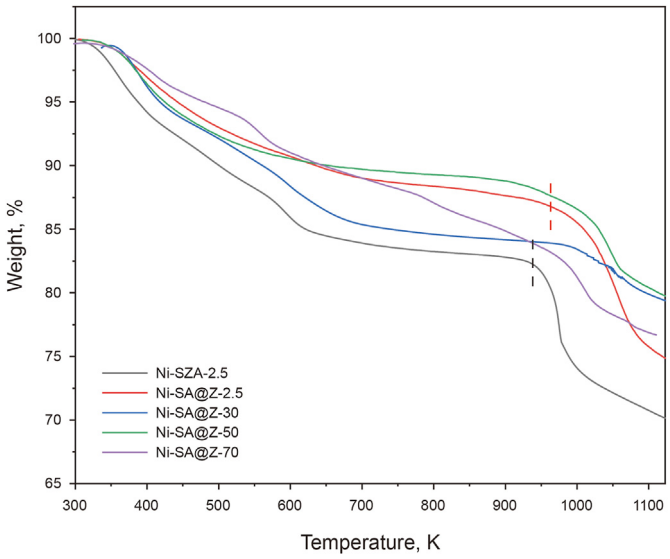

Fig. 3. TG curves of Ni-SZA-2.5 and Ni-SA@Z-*x* catalysts.

decomposition of persulfate species of Ni-SA@Z-*x* was shifted to higher temperatures of 963 K. These observations suggest that persulfate anions on the surface of Ni-SA@Z-*x* were bonded more strongly to dehydrated zirconia, leading to the increased thermal stability of superacid. This will be further discussed in Section 3.9.

3.5. FTIR

The FTIR spectrum of fresh catalysts was depicted in Fig. 4. All the samples showed similar peaks, the bands at 3422 and 1630 cm^{-1} were assigned to the physically adsorbed water molecules and the bending mode (δ_{HOH}) of coordinated molecular water associated with the persulfate group, respectively (Sarkar et al., 2007). The bands at 1156 and 1077 cm^{-1} were assigned to the symmetric O–S–O stretching mode of bidentate persulfate ions coordinated to the metal ion, which was responsible for the Lewis acid sites in persulfated zirconia samples. The band at 1255 cm^{-1} corresponded to the antisymmetric O=S=O stretching frequency of persulfate ions bonded to ZrO_2, which was responsible for the Brønsted acid sites in persulfated zirconia samples (Mishra et al., 2003). These three bands appearing at about 1077, 1156 and 1255 cm^{-1} were assigned to bidentate S ions coordinated to ZrO_2 in C_2v symmetry with a ν3 vibration, indicating the formation of a strongly superacid structure (Yadav and Murkute, 2004). The intensity and degree of splitting of the persulfate bands reflect the proportion of acid sites of the catalyst. The Ni-SA@Z-2.5 catalyst exhibited three vibration bands corresponding to S=O and S–O bond, which showed higher intensity and degree of splitting than those of Ni-SZA-2.5. This indicated that the Ni-SA@Z-2.5 provided more acid sites and stronger acidity, as further confirmed by Py-IR results (see Section 3.6). With increasing Al content, the intensity and the degree of splitting of the vibrational bands corresponding to S=O (1255 cm^{-1}) and S–O (1077 cm^{-1} and 1156 cm^{-1}) of Ni-SA@Z-*x* increased, and the Ni-SA@Z-30 possessed the highest intensity and the splitting degree among Ni-SA@Z-*x*.

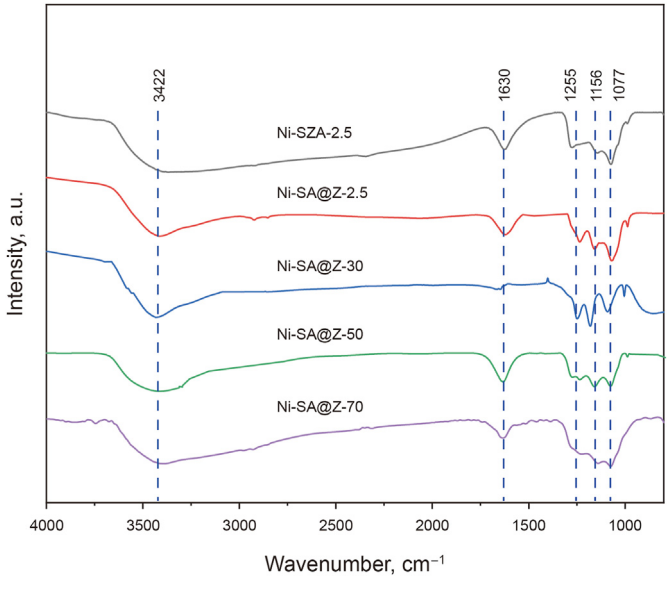

Fig. 4. FTIR spectrum of Ni-SZA-2.5 and Ni-SA@Z-*x* catalysts.

3.6. Py-IR

The Py-IR results of fresh and spent catalysts were listed in Tables S1 and S2. All of the catalysts possessed more Lewis acid sites than Brønsted acid sites, and both of them decreased with increasing desorption temperature. Compared with Ni-SZA-2.5, distinct increases in the amount of Brønsted and Lewis acid sites could be observed for Ni-SA@Z-2.5, which possessed smaller (Table 1) and more uniformly dispersed ZrO_2 particles (Fig. 2 TEM) on the surface of mesoporous Al_2O_3 nanoparticles, facilitating interaction with $S_2O_8^{2-}$ anions to generate acid sites. With increasing Al content, all the amounts of Lewis acid sites and Brønsted acid sites for Ni-SA@Z-*x* increased remarkably. These results indicated that the addition of Al improved the stability of the persulfate loaded on the surface to form stronger acid sites. Foo et al. (2015) proposed that the Brønsted acidity was associated with persulfuric acid clusters on zirconia. With increasing Al content, the persulfate anions were bonded more strongly to dehydrated zirconia (as shown in TG analysis) and thus formed more superacid sites.

For all of the spent catalysts (Table S2), the amount of Brønsted acid sites and Lewis acid sites were both decreased as compared to the corresponding fresh one. However, the amount of Brønsted acid sites decreased more significantly than that of Lewis acid sites, implying that the former were the main active acid sites for isomerization (Yang and Weng, 2010). For Ni-SZA-2.5, the strong acid sites had completely disappeared after reaction. However, the spent Ni-SA@Z-2.5 still possessed the strong acid sites. In addition, the amounts of weak, moderate, and strong acid sites on Ni-SA@Z-*x* ($x < 50$) were still maintained at high levels after reaction. This can be attributed to a stabilizing effect of Al on S species on the catalyst surface and some suppression of the loss of acid sites (Hou et al., 2017). Analysis of the bulk sulfur content also confirmed it (Table S3, Section 3.8).

3.7. XPS

The surficial chemical composition of the catalysts was investigated by XPS analysis. As shown in Fig. 5(a), the full-scan XPS spectrum shows that the Ni-SZA-2.5 and Ni-SA@Z-*x* contains Ni, Zr, Al, S and O species, respectively. In Fig. 5(b), the high-resolution S 2p spectrum consists of two contributions for all the samples. The peak centered at 169.1 eV can be assigned to S^{6+} species of peroxydisulfate (Shanthi et al., 2019). Sulfur with an oxidation state of +6 is known to be the most active and essential for the formation of solid superacid sites. While the peak appeared at 170.4–169.9 eV

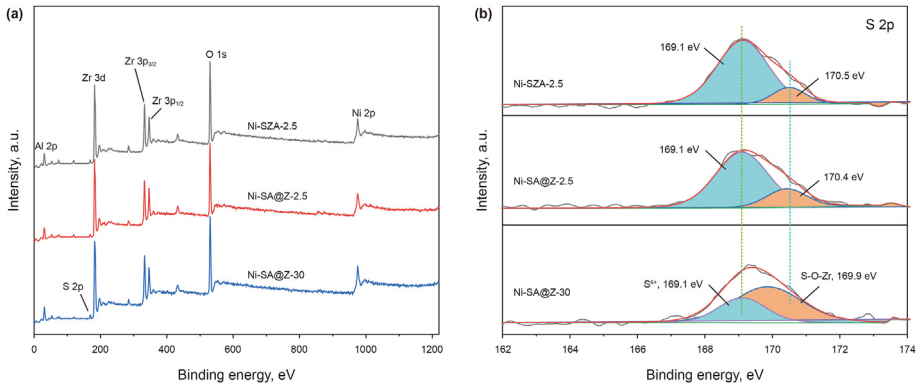

Fig. 5. (**a**) Full-scan and (**b**) high-resolution S 2p XPS spectrum of typical samples.

can be attributed to S—O—Zr bond. As compared to the Ni-SZA-2.5 and Ni-SA@Z-2.5, the binding energy of Ni-SA@Z-30 shifted to lower value, indicating that the electronic environment of S has changed when the Al content raised to 30 wt% (Wang et al., 2018).

3.8. Elemental analysis

Table S3 showed the atomic contents obtained from XRF, XPS and carbon-sulfur analysis. The Ni contents of all of the catalysts were roughly equal to the stoichiometric content. In addition, compared to the fresh catalysts, no significant change was observed after reaction, showing that deactivation of the catalyst was not caused by the Ni leaching loss. Compared with Ni-SZA-2.5 (1.74 wt %), the sulfur content of the Ni-SA@Z-2.5 increased to a slightly higher value of 2.36 wt%, indicating that Ni-SA@Z-2.5 could stabilize more S species, as discussed in Section 3.7. With incremental Al content, the sulfur content further increased and the sulfur content of Ni-SA@Z-50 reached up to 3.41 wt%. After reaction, both Ni-SZA-2.5 and Ni-SA@Z-*x* catalysts underwent an overt sulfur loss. Many researchers (Yang and Weng, 2009; Saha and Sengupta, 2015) have found that the loss of loosely bound S species during reaction resulted in catalyst deactivation. Besides, for Ni-SZA-2.5, significant carbon deposition occurred during isomerization (0.45 wt%). The amount of carbon deposition on the spent Ni-SA@Z-*x* samples was improved as compared to that of the spent Ni-SZA-2.5, which supported the view that the larger mesopore volume of the core-shell catalysts effectively enhanced the diffusion rate and inhibited carbon deposition. Thus, it can be speculated that the Ni-SA@Z-*x* catalysts would exhibit excellent thermal stability (Kuznetsov et al., 2017) (see Scheme 1).

3.9. Catalytic properties

The Ni-SZA-2.5 and Ni-SA@Z-*x* catalysts have been tested in the isomerization of *n*-pentane at a pressure of 2.0 MPa, an H_2/*n*-pentane molar ratio of 4.0, and a WHSV of 1.0 h^{-1} and results were illustrated in Fig. 6 and Fig. S3. The catalytic activities of all of the catalysts first increased and reached a maximum, and then decreased with increasing temperature. The raw Ni-SZA-2.5 showed a maximum isopentane yield of 60.3% at optimized temperature (Fig. S3). For Ni-SA@Z-2.5, the isopentane yield of 65.6% was reached at 473 K. With increasing the Al content, the optimum temperature decreased and then increased. The Ni-SA@Z-30 possessed the lowest optimum temperature at 453 K with the high isopentane yield of 64.7%. Possible reasons to explain the high isopentane yield of Ni-SA@Z-30 catalyst at lower temperature may be as follows (Scheme 2). (i) More and stronger superacid sites are formed featured by the FTIR and Py-IR analysis (Table S1 and Fig. 5). In particular, the amount of strong Brønsted acid sites of Ni-SA@Z-30 was 6.0 and 54.3 times higher than that of Ni-SA@Z-2.5 and Ni-SZA-2.5, respectively. (ii) Better dispersion of active acid and metal sites was achieved due to the high surface area (Table 1). However, further increased Al content resulted in an adverse activity, which led to higher reaction temperature and downtrend in isopentane yield. According to Kamoun et al. (2015), addition of excessive Al to Ni/ZrO_2–SO_4^{2-} have the negative effect of the Al on isomerization

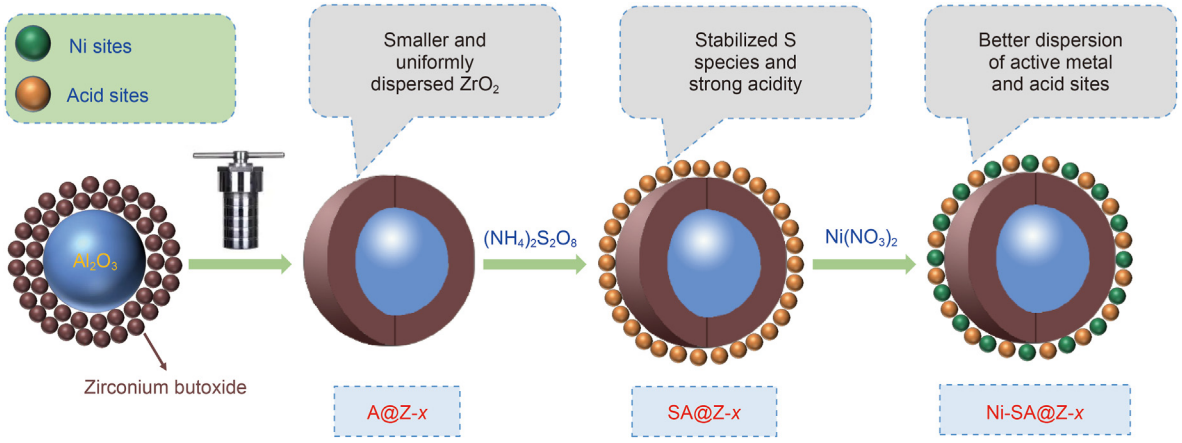

Scheme 1. Schematic diagram for the synthesis of Ni-SA@Z-*x*

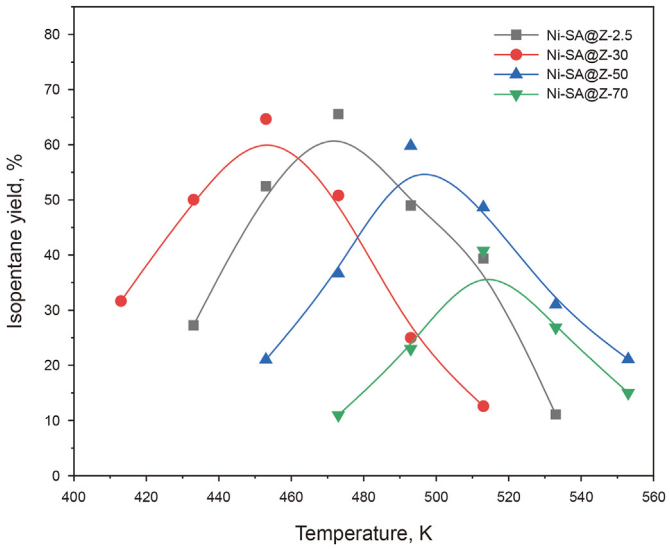

Fig. 6. Catalytic activity of Ni-SA@Z-*x* catalysts.

activity at low temperature. Similar results have been reported in our previous study (Song et al., 2014), which showed that the isopentane yield over Pd-SZA-2.5 (Al content of 2.5%) was 64.3% at 511 K, however, when the amount of Al content increased to 5 wt%, the optimum temperature increased to 553 K with a sharp decline in isopentane yield. This can be attributed to the decrease in the tetragonal phase and its crystallinity at a higher Al content.

(Reaction condition: p = 2.0 MPa, H_2/*n*-pentane molar ratio = 4.0, WHSV = 1.0 h^{-1}).

Fig. 7 showed the stability results for Ni-SZA-2.5 and Ni-SA@Z-*x* over a period of 5000 min at their corresponding optimum reaction temperatures with other conditions maintained the same. The isopentane yield of the Ni-SZA-2.5 catalyst showed an obvious decline during isomerization, which decreased dramatically from 60.3% to 20.0% (decreased by 66.8%) after 1500 min. Compared to traditional Ni-SZA-2.5 catalysts, the Ni-SA@Z-2.5 exhibited much better stability, and the isopentane yield showed a slight decreased from 65.4% to 60.2% (decreased by 7.7%) after 1500 min and to 50.1% (decreased by 23.1%) after 5000 min. The Ni-SA@Z-30 catalyst exhibited the most promising catalytic performance and showed a high isopentane yield of approximately 63.1% with no or tiny deactivation after 5000 min. Possible reasons may be proposed to explain the great stability of the Ni-SA@Z-*x* catalyst for *n*-pentane isomerization (Scheme 2). (i) The pore sizes and volumes of the catalysts increased in the order: Ni-SZA-2.5 (3.7 nm, 0.089 $cm^3\ g^{-1}$) < Ni-SA@Z-2.5 (5.6 nm, 0.103 $cm^3\ g^{-1}$) < Ni-SA@Z-30 (6.9 nm, 0.214 $cm^3\ g^{-1}$) (Table 1). The large pore size and pore volume enhanced the diffusion rates of the reactant and products and largely suppressed carbon deposition. This was confirmed by analysis of carbon deposition on the spent samples. The amounts of carbon deposited on the spent Ni-SA@Z-2.5 and Ni-SA@Z-30 were only 0.07 wt% and 0.05 wt%, respectively, much lower than that of spent Ni-SZA-2.5 (0.45 wt%, Table S3). The color changes of the catalysts after reaction also supported this (Fig. 7). (ii) The loss of sulfur entities can be suppressed for Ni-SA@Z-*x*. The ZrO_2 shell, which consists of more and smaller tetragonal ZrO_2 particles because of the large surface area of the Al_2O_3 core (Table 1), ensured intimate contact between Zr and S. Therefore, the superacid became more stable in thermally (See TG analysis). Elemental analysis showed that the sulfur content of Ni-SA@Z-2.5 and Ni-SA@Z-30 catalysts decreased by 16.1 and 18.1% after reaction for 5000 min on stream, respectively, whereas the Ni-SZA-2.5 underwent a higher sulfur loss of 27.6% after 1500 min (Table S3). Therefore, the deactivation of the catalysts caused by sulfur removal was somewhat suppressed for Ni-SA@Z-*x*. (iii) For the Ni-SZA-2.5 catalyst, the strong Brønsted acid sites, which played an important role in isomerization (Li et al., 2020), completely disappeared after reaction (Table S2). As contrast, the content of Brønsted acid for the spent Ni-SA@Z-2.5 and Ni-SA@Z-30 was 0.6 μmol g^{-1} and 6.5 μmol g^{-1}, respectively. In addition, the contents of weak, moderate, and strong acid sites of Ni-SA@Z-30 still maintained to a great extent after reaction.

(Reaction condition: p = 2.0 MPa, H_2/*n*-pentane molar ratio = 4:1, WHSV = 1.0 h^{-1}).

4. Conclusion

This study paved a new path for the synthesis of highly active and highly stable non-noble Ni-SA@Z-*x* catalysts for *n*-pentane isomerization. The Ni-SA@Z-30 provided a sustained high isopentane yield (64.7%) with little or no deactivation within 5000 min at a low temperature of 453 K. The high isopentane yield of Ni-SA@Z-30 can be attributed to the formation of more and

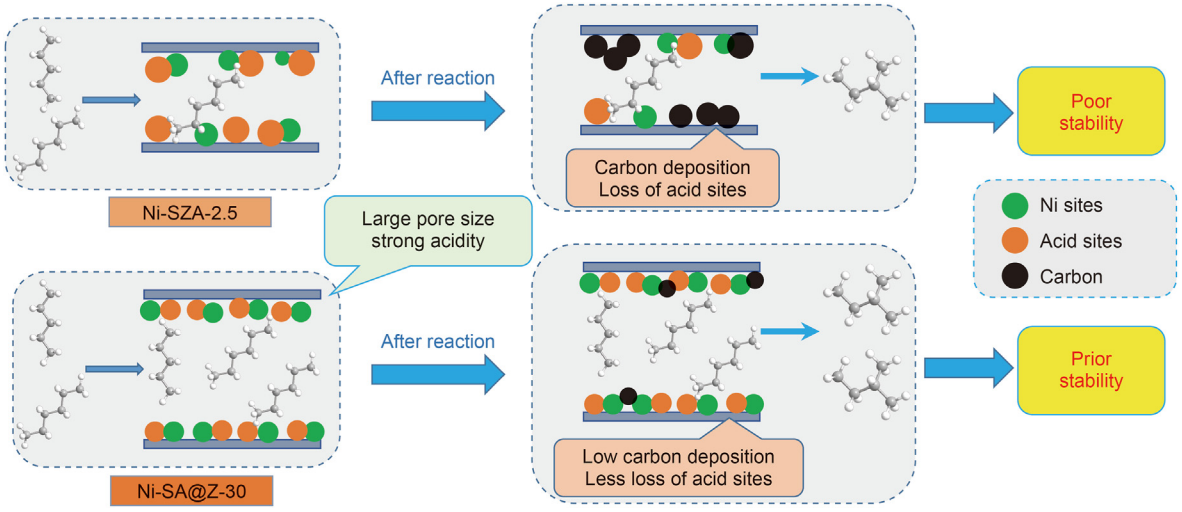

Scheme 2. Possible reasons of high stability for Ni-SA@Z-30 as compared to Ni-SZA-2.5 catalyst.

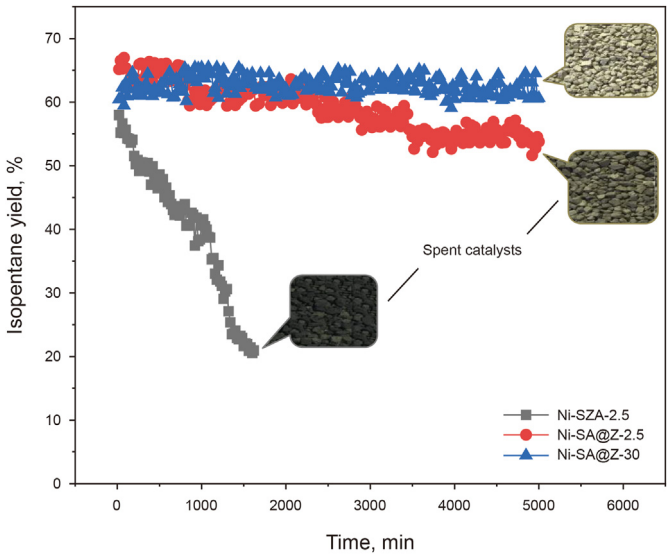

Fig. 7. Stability test of Ni-SZA-2.5, Ni-SA@Z-*x* catalysts at their optimum temperatures.

stronger superacid sites due to numerous small tetragonal ZrO_2 particles derived from ZrO_2 shell and better dispersion of active acid and metal sites. The excellent stability can be attributed to the following factors: (i) carbon deposition was greatly suppressed by the large pore size and huge pore volume; (ii) the loss of sulfur entities was suppressed due to the stronger interaction between small tetragonal ZrO_2 particles and S species; (iii) the loss of strong Brønsted acid sites was improved during the isomerization reaction. To the best of our knowledge, such a non-noble superacid catalyst with high isopentane yield and excellent stability at a low pressure (2.0 MPa) is extremely unusual and being reported for the first time.

Appendix A. Supplementary data

Supplementary data to this article can be found online at https://doi.org/10.1016/j.petsci.2023.02.027.

References

Arkatova, L.A., 2010. The deposition of coke during carbon dioxide reforming of methane over intermetallides. Catal. Today 157 (1–4), 170–176. https://doi.org/10.1016/j.cattod.2010.03.003.

Bang, J.H., Lee, N., Mirzaei, A., et al., 2020. Exploration of ZrO_2-shelled nanowires for chemiresistive detection of NO_2 gas. Sensor. Actuator. B Chem. 319, 128309. https://doi.org/10.1016/j.snb.2020.128309.

Das, S., Jangam, A., Jayaprakash, S., et al., 2021. Role of lattice oxygen in methane activation on Ni-phyllosilicate@$Ce_{1-x}Zr_xO_2$ core-shell catalyst for methane dry reforming: Zr doping effect, mechanism, and kinetic study. Appl. Catal. B Environ. 290, 119998. https://doi.org/10.1016/j.apcatb.2021.119998.

Foo, R., Vazhnova, T., Lukyanov, D.B., et al., 2015. Formation of reactive Lewis acid sites on Fe/WO_3-ZrO_2 catalysts for higher temperature SCR applications. Appl. Catal. B Environ. 162, 174–179. https://doi.org/10.1016/j.apcatb.2014.06.034.

Gao, J., Ma, R., Feng, L., et al., 2021. Ambient hydrogenation and deuteration of alkenes using a nanostructured Ni-Core-Shell Catalyst. Angew. Chem. 133 (34), 18739–18746. https://doi.org/10.1002/ange.202105492.

Gao, Z., Xia, Y., Hua, W., et al., 1998. New catalyst of SO_4^{2-}/Al_2O_3-ZrO_2 for *n*-butane isomerization. Top. Catal. 6 (1), 101–106. https://doi.org/10.1023/A:1019122608037.

González, M.R., Fogash, K.B., Kobe, J.M., et al., 1997. Promotion of *n*-butane isomerization by hydroxyl groups on sulfated zirconia. Catal. Today 33 (1–3), 303–312. https://doi.org/10.1016/S0920-5861(96)00156-3.

Hou, X., Qiu, Y., Yuan, E., et al., 2017. Promotion on light olefins production through modulating the reaction pathways for *n*-pentane catalytic cracking over ZSM-5 based catalysts. Appl. Catal. Gen. 543, 51–60. https://doi.org/10.1016/j.apcata.2017.06.013.

Hua, W., Xia, Y., Yue, Y., et al., 2000. Promoting effect of Al on SO_4^{2-}/M_xO_y (M= Zr, Ti, Fe) catalysts. J. Catal. 196 (1), 104–114. https://doi.org/10.1006/jcat.2000.3032.

Joo, J.B., Vu, A., Zhang, Q., et al., 2013. A sulfated ZrO_2 hollow nanostructure as an acid catalyst in the dehydration of fructose to 5-hydroxymethylfurfural. ChemSusChem 6 (10), 2001–2008. https://doi.org/10.1002/cssc.201300416.

Kamoun, N., Younes, M.K., Ghorbel, A., et al., 2015. Comparative study of aerogels nanostructured catalysts: Ni/ZrO_2-SO_4^{2-} and Ni/ZrO_2-Al_2O_3-SO_4^{2-}. Ionics 21 (1), 221–229. https://doi.org/10.1007/s11581-014-1168-2.

Kim, S.Y., Goodwin Jr., J.G., Galloway, D., 2000. *n*-Butane isomerization on sulfated zirconia: active site heterogeneity and deactivation. Catal. Today 63 (1), 21–32. https://doi.org/10.1016/S0920-5861(00)00442-9.

Kim, S.Y., Lohitharn, N., Goodwin Jr., J.G., et al., 2006. The effect of Al_2O_3-promotion of sulfated zirconia on *n*-butane isomerization: an isotopic transient kinetic analysis. Catal. Commun. 7 (4), 209–213. https://doi.org/10.1016/j.catcom.2005.11.005.

Kuznetsov, P.N., Obukhova, A.V., Kuznetsova, L.I., et al., 2017. A study of Pt/WO_4^{2-}/ZrO_2 catalyst deactivation in the hydroisomerization of heptane and a heptane-benzene mixture. Petrol. Chem. 57 (5), 403–409. https://doi.org/10.1134/S0965544117050073.

Li, C., Stair, P.C., 1996. Ultraviolet Raman spectroscopy characterization of sulfated zirconia catalysts: fresh, deactivated and regenerated. Catal. Lett. 36 (3), 119–123. https://doi.org/10.1007/BF00807606.

Li, T., Zhang, L., Tao, Z., et al., 2020. Synthesis and characterization of amorphous silica-alumina with enhanced acidity and its application in hydro-isomerization/cracking. Fuel 279, 118487. https://doi.org/10.1016/j.fuel.2020.118487.

Li, X., Nagaoka, K., Olindo, R., et al., 2006. Synthesis of highly active sulfated zirconia by sulfation with SO_3. J. Catal. 238 (1), 39–45. https://doi.org/10.1016/j.jcat.2005.11.039.

Liu, E., Locke, A.J., Martens, W.N., et al., 2012. Fabrication of macro-mesoporous zirconia-alumina materials with a one-dimensional hierarchical structure. Cryst. Growth Des. 12 (3), 1402–1410. https://doi.org/10.1021/cg201502h.

Liu, N., Ma, Z., Wang, S., et al., 2020. Palladium-doped sulfated zirconia: deactivation behavior in isomerization of *n*-hexane. Fuel 262, 116566. https://doi.org/10.1016/j.fuel.2019.116566.

Lyu, Y., Zhan, W., Yu, Z., et al., 2021. One-pot synthesis of the highly efficient bifunctional Ni-SAPO-11 catalyst. J. Master. Sci. Technol. 76, 86–94. https://doi.org/10.1016/j.jmst.2020.10.033.

Mishra, M.K., Tyagi, B., Jasra, R.V., 2003. Effect of synthetic parameters on structural, textural, and catalytic properties of nanocrystalline sulfated zirconia prepared by sol-gel technique. Ind. Eng. Chem. Res. 42 (23), 5727–5736. https://doi.org/10.1021/ie030099t.

Mokari, T., Sztrum, C.G., Salant, A., et al., 2005. Formation of asymmetric one-sided metal-tipped semiconductor nanocrystal dots and rods. Nat. Mater. 4 (11), 855–863. https://doi.org/10.1038/nmat1505.

Ng, F.T.T., Horvát, N., 1995. Sulfur removal from ZrO_2/SO_4^{2-} during *n*-butane isomerization. Appl. Catal. Gen. 123 (2), L197–L203. https://doi.org/10.1016/0926-860X(95)00025-9.

Nichele, V., Signoretto, M., Menegazzo, F., et al., 2012. Glycerol steam reforming for hydrogen production: design of Ni supported catalysts. Appl. Catal. B Environ. 111, 225–232. https://doi.org/10.1016/j.apcatb.2011.10.003.

Reddy, C.V., Babu, B., Reddy, I.N., et al., 2018. Synthesis and characterization of pure tetragonal ZrO_2 nanoparticles with enhanced photocatalytic activity. Ceram. Int. 44 (6), 6940–6948. https://doi.org/10.1016/j.ceramint.2018.01.123.

Saha, B., Sengupta, S., 2015. Influence of different hydrocarbon components in fuel on the oxidative desulfurisation of thiophene: deactivation of catalyst. Fuel 150, 679–686. https://doi.org/10.1016/j.fuel.2015.02.078.

Sarkar, D., Mohapatra, D., Ray, S., et al., 2007. Synthesis and characterization of sol-gel derived ZrO_2 doped Al_2O_3 nanopowder. Ceram. Int. 33 (7), 1275–1282. https://doi.org/10.1016/j.ceramint.2006.05.002.

Satam, J.R., Jayaram, R.V., 2008. Selective procedure for the conversion of alcohols into alkyl iodides with SO_4^{2-}/ZrO_2 and NaI at room temperature. Catal. Commun. 9 (6), 1033–1039. https://doi.org/10.1016/j.catcom.2007.10.004.

Shanthi, P.M., Hanumantha, P.J., Ramalinga, K., et al., 2019. Sulfonic acid based complex framework materials (CFM): nanostructured polysulfide immobilization systems for rechargeable lithium-sulfur battery. J. Electrochem. Soc. 166 (10), A1827–A1835. https://doi.org/10.1149/2.0251910jes.

Song, H., Wang, N., Song, H., et al., 2014. Effect of Al content on the isomerization performance of solid superacid Pd-$S_2O_8^{2-}$/ZrO_2-Al_2O_3. Chin. J. Chem. Eng. 22 (11–12), 1226–1231. https://doi.org/10.1016/j.cjche.2014.07.002.

Song, H., Wang, N., Song, H., et al., 2015. La-Ni modified $S_2O_8^{2-}$/ZrO_2-Al_2O_3 catalyst in *n*-pentane hydroisomerization. Catal. Commun. 59, 61–64. https://doi.org/10.1016/j.catcom.2014.09.037.

Song, H., Wang, N., Song, H., et al., 2016a. Effect of Pd content on the isomerization performance over Pd-$S_2O_8^{2-}$/ZrO_2-Al_2O_3 catalyst. Res. Chem. Intermed. 42, 951–962. https://doi.org/10.1007/s11164-015-2065-7.

Song, H., Zhao, L., Wang, N., et al., 2016b. Isomerization of *n*-pentane over La-Ni-$S_2O_8^{2-}$/ZrO_2-Al_2O_3 solid superacid catalysts: deactivation and regeneration. Appl. Catal. Gen. 526, 37–44. https://doi.org/10.1016/j.apcata.2016.08.003.

Thommes, M., Kaneko, K., Neimark, A.V., et al., 2015. Physisorption of gases, with special reference to the evaluation of surface area and pore size distribution (IUPAC technical report). Pure Appl. Chem. 87, 9–10. https://doi.org/10.1515/pac-2014-1117.

Wang, P., Yue, Y., Wang, T., et al., 2020. Alkane isomerization over sulfated zirconia solid acid system. Int. J. Energy Res. 44 (5), 3270–3294. https://doi.org/10.1002/er.4995.

Wang, P., Zhang, J., Wang, G., et al., 2016. Nature of active sites and deactivation mechanism for *n*-butane isomerization over alumina-promoted sulfated

zirconia. J. Catal. 338, 124–134. https://doi.org/10.1016/j.jcat.2016.02.027.
Wang, S., Yin, T., Meng, X., et al., 2022. Synthesis of Al-incorporated sulfated zirconia with improved and stabilized surface sulfur species for removal of trace olefins from aromatics. Catal. Sci. Techol. 12 (1), 212–225. https://doi.org/10.1039/D1CY01443A.
Wang, Y., Yao, L., Wang, Y., et al., 2018. Low-temperature catalytic CO_2 dry reforming of methane on Ni-Si/ZrO_2 catalyst. ACS Catal. 8 (7), 6495–6506. https://doi.org/10.1021/acscatal.8b00584.
Yadav, G.D., Murkute, A.D., 2004. Preparation of a novel catalyst UDCaT-5: enhancement in activity of acid-treated zirconia-effect of treatment with chlorosulfonic acid vis-à-vis sulfuric acid. J. Catal. 224 (1), 218–223. https://doi.org/10.1016/j.jcat.2004.02.021.
Yang, X., Wang, X., Gao, G., et al., 2013. Nickel on a macro-mesoporous Al_2O_3@ZrO_2 core/shell nanocomposite as a novel catalyst for CO methanation. Int. J. Hydrogen Energy 38 (32), 13926–13937. https://doi.org/10.1016/j.ijhydene.2013.08.083.
Yang, Y., Weng, H., 2009. The role of H_2 in *n*-butane isomerization over Al-promoted sulfated zirconia catalyst. J. Mol. Catal. Chem. 304 (1–2), 65–70. https://doi.org/10.1016/j.molcata.2009.01.025.
Yang, Y., Weng, H., 2010. Al-promoted Pt/SO_4^{2-}/ZrO_2 with low sulfate content for *n*-heptane isomerization. Appl. Catal. Gen. 384 (1–2), 94–100. https://doi.org/10.1016/j.apcata.2010.06.010.
Zarubica, A., Krstić, J.B., Popović, D., et al., 2021. Influence of alumina addition on structural and catalytic properties of sulphated zirconia in isomerization of n-hexane. Process. Appl. Ceram. 15 (2), 111–119. https://doi.org/10.2298/PAC2102111Z.
Zhan, W., Lyu, Y., Liu, X., et al., 2022. The direct synthesis of Ni/SAPO-11 hydroisomerization catalyst via a novel two-step crystallization strategy. Petrol. Sci. 19 (5), 2448–2459. https://doi.org/10.1016/j.petsci.2022.01.014.
Zhao, J., Yue, Y., Hua, W., et al., 2007. Catalytic activities and properties of mesoporous sulfated Al_2O_3–ZrO_2. Catal. Lett. 116 (1), 27–34. https://doi.org/10.1007/s10562-007-9085-x.
Zhou, S., Song, Y., Zhao, J., et al., 2021. Study on the mechanism of water poisoning Pt-promoted sulfated zirconia alumina in *n*-hexane isomerization. Energy Fuel. 35 (18), 14860–14867. https://doi.org/10.1021/acs.energyfuels.1c01440.
Zhou, S., Song, Y., Zhao, J., et al., 2022. Impacts of alumina introduction on a Pt-SO_4/ZrO_2 catalyst in light naphtha isomerization. Ind. Eng. Chem. Res. 61 (3), 1285–1293. https://doi.org/10.1021/acs.iecr.1c03040.